

This item was submitted to [Loughborough's Research Repository](#) by the author.  
Items in Figshare are protected by copyright, with all rights reserved, unless otherwise indicated.

## **Influence of microstructure on cavitation in the heat affected zone of a Grade 92 steel weld during long-term high temperature creep**

PLEASE CITE THE PUBLISHED VERSION

<https://doi.org/10.1016/j.matchar.2020.110663>

PUBLISHER

Elsevier BV

VERSION

AM (Accepted Manuscript)

PUBLISHER STATEMENT

This paper was accepted for publication in the journal Materials Characterization and the definitive published version is available at <https://doi.org/10.1016/j.matchar.2020.110663>.

LICENCE

CC BY-NC-ND 4.0

REPOSITORY RECORD

Xu, X, JA Siefert, JD Parker, and Rachel Thomson. 2020. "Influence of Microstructure on Cavitation in the Heat Affected Zone of a Grade 92 Steel Weld During Long-term High Temperature Creep". Loughborough University. <https://hdl.handle.net/2134/13101809.v1>.

# **Influence of microstructure on cavitation in the heat affected zone of a Grade 92 steel weld during long-term high temperature creep**

**X. Xu<sup>1\*</sup>, J.A. Siefert<sup>2</sup>, J.D. Parker<sup>2</sup> and R.C. Thomson<sup>1\*\*</sup>**

<sup>1</sup>Department of Materials, Loughborough University, Loughborough, LE11 3TU, UK

<sup>2</sup>EPRI, 1300 Harris Boulevard, Charlotte, North Carolina, 28262, USA

\*Corresponding author: xu.xu@manchester.ac.uk

\*\* Corresponding author: r.c.thomson@lboro.ac.uk

## **Keywords**

9% Cr tempered martensitic steel, heat affected zone, high temperature creep, creep cavitation, welding

## **Highlights:**

- Creep damage in the heat affected zone of a multi-pass Grade 92 steel weld was evaluated after long-term creep exposure.
- Creep damage was compared with the variation of microstructure in the heat affected zone.
- Cavitation preferentially occurs in the regions showing a refined microstructure with an inhomogeneous distribution of the  $M_{23}C_6$  carbides.
- Creep cavities are preferentially formed on the  $Al_2O_3$ , MnS and BN particles.
- The partially transformed zones are the most susceptible to creep cavitation.

## **Abstract**

The microstructure in the heat affected zone of the multi-pass welds constructed by using the 9% Cr tempered martensitic steels is complex and susceptible to premature creep failure. In the present research, a systematic investigation has been conducted after long-term creep

exposure in the heat affected zone of a multi-pass weld on the 9% Cr Grade 92 steel to identify the sub-optimal microstructures with a high susceptibility to creep cavitation. The characterisation techniques employed include hardness mapping and a range of electron-based microscopy techniques to provide quantitative data of microstructure and creep cavity. In this case, preferential creep cavitation has been confirmed in the regions within the heat affected zone that possess a microstructure with an inhomogeneous distribution of the  $M_{23}C_6$  carbides and a refined martensitic grain structure. Creep cavities have been observed on the secondary phase particles including the  $Al_2O_3$ , the MnS and the BN phases. In addition, no clear trends have been observed between creep cavity and the variation of hardness or the Laves phase particles in the heat affected zone. The observations from the current research confirm that creep cavitation preferentially occurs in the partially-transformed zones that were subjected to thermal cycles associated with peak temperatures between the  $Ac_1$  and the  $Ac_3$  transus temperatures during weld fabrication.

## **1. Introduction**

The 9% Cr tempered martensitic steels have been used in a range of applications in the power generation industry because of their excellent creep strength and good corrosion resistance. These materials are usually used to construct the components in the steam pipeline system such as pipes, tubes and headers [1]. The thermo-mechanical processing utilised for the fabrication of the industrial components normally involves forging, normalisation and tempering. In addition, sophisticated multi-pass welding technique is commonly used for thick-section applications to produce complicated welds with satisfactory mechanical properties for long-term applications at elevated temperatures > 550 °C [2,3]. The 9% Cr steels are compatible with a range of welding processes available for industrial applications including Sub-merged Arc Weld (SAW), Gas Tungsten Arc Welding (GTAW) and Shielded Metal Arc Welding (SMAW) [2].

The microstructure of the 9% Cr steels is typically composed of a tempered martensitic matrix in combination with the strengthening precipitate particles that are evenly distributed on grain boundaries and within the grain interiors [1]. However, the

microstructure within the Heat Affected Zone (HAZ) of weldments is extremely complex due to the complicated thermal and stress experiences for the local materials during welding. The microstructural regions that arise in the HAZ are commonly categorised based on the variation of grain size into the Coarse Grain (CG), Fine Grain (FG), Inter-Critical (IC) and Sub-Critical (SC) regions [4,5]. This description of the HAZ provides a generalised classification of microstructure in the weldments made from low alloy ferritic and bainitic steels, and have continued to be adopted in the studies on the family of 9-12 wt. % Cr steel weldments [5–7].

The premature creep failure occurred in the HAZ is a known problem to 9% Cr steel welds, in which creep cavitation preferentially takes place in the HAZ regions that are close to the boundary with the parent metal [4,5,8,9]. The effect of microstructure on creep cavitation has been extensively investigated to understand the factors contributing to the formation of cavities in the HAZ. For instance, it is revealed that cavitation is promoted in the regions showing low hardness and a refined grain structure [10–12]. Creep cavitation is also promoted in the regions showing an inhomogeneous distribution of strengthening precipitate particles on lath and grain boundaries [13–17]. In addition, the secondary phase particles above a critical size are also related to creep cavitation as they act as the preferred sites for cavity nucleation [16–22]. These detrimental phases include the  $\text{Al}_2\text{O}_3/\text{MnS}$  inclusions, the BN phases and the  $\text{M}_{23}\text{C}_6$  carbides or the Laves phases that are coarsened during creep [17,18,21]. In particular, cavities are preferentially developed on the BN particles in the HAZ of Grade 92 steel welds [22]. These cavities formed in the early stage of creep significantly deteriorate creep ductility and are coalesced to form macro-cracks at the end of creep life [22].

Detailed metallographic observations in the existing studies on 9% Cr steel welds have provided the basis for understanding premature creep failure in the HAZ, while the key factors contributing to cavitation are still under debate and not completely understood. For instance, creep tests conducted at different temperature and stress conditions indicate that creep failure is not always occurred in the HAZ regions showing the lowest hardness [5,23,24]. Other studies also demonstrate the cases of weldments not ruptured in the regions

possessing the most refined grain structure [25,26]. In addition, there is a lack of a systematic study to identify typical characteristics of sub-optimal microstructures being susceptible to cavitation with a clear link to the thermal experiences during welding.

To understand the critical link with the history of thermal experiences, the microstructure in the HAZs of Grade 92 steel welds has been systematically investigated to correlate with bulk materials after the thermal experiences that simulate typical thermal cycles during welding [15,27]. These systematic observations have led to a detailed description for the microstructure in the HAZ that is divided into three distinct regions: the Completely Transformed Zone (CTZ), the Partially Transformed Zone (PTZ) and the Over-Tempered Zone (OTZ) [15]. The microstructure of the CTZ is produced upon a weld thermal cycle associated with a peak temperature above the  $Ac_3$  transus temperature, giving rise to a fully re-austenitised martensitic matrix and a complete dissolution of the pre-existing precipitate particles. The PTZ experiences a thermal cycle associated with an inter-critical peak temperature between the  $Ac_1$  and the  $Ac_3$  temperatures, which leads to a partially re-austenitised martensitic matrix together with partial dissolution of the pre-existing precipitates. The OTZ has a grain structure that is similar to the original matrix in the parent metal, whilst the pre-existing precipitate particles are slightly coarsened after experiencing thermal cycles with a peak temperature below the  $Ac_1$  temperature [15]. As such, an accurate description of the HAZ microstructure in Grade 92 steel welds has been established by classifying the HAZ into three regions that are related to where the peak temperature of weld thermal cycles in relation to the  $Ac_1$  and the  $Ac_3$  temperatures.

Following the previous studies detailing the initial microstructure in the as-fabricated condition, the present research systematically investigates the microstructure in the HAZ of Grade 92 steel welds after long-term creep exposure. This, in turn, establishes the critical link between the initial and ex-service microstructures and facilitates a clear definition for the regions being the most susceptible to cavitation in the HAZ of multi-pass Grade 92 steel welds. The characterisation techniques employed include hardness mapping and a range of electron-based microscopy techniques to provide quantitative data of microstructure and

creep damage. The correlation between creep damage and microstructure leads to a clear identification of the critical metallurgical factors related with the formation of cavities.

## 2. Materials and experimental procedure

### 2.1. Materials

A circumferential multi-pass weld joint was fabricated in the Grade 92 steam pipe using the typical procedures utilised for industrial applications. The heat treatment of the pipe material involves a normalisation process at 1065 °C and a tempering process at 777 °C. The chemical composition of the material was examined by using the Inductively Coupled Plasma (ICP) analysis with the results detailed in Table 1.

**Table 1. Experimentally measured chemical composition (wt. %) of the bulk material in a thick-section Grade 92 steam pipe using ICP-OE and ICP-MS, the balance is Fe.**

Cr	Mn	Mo	Nb	Ni
8.860	0.490	0.420	0.074	0.400
N	Al	Cu	P	S
0.047	0.006	0.160	0.015	0.003
Si	V	W	C	B
0.270	0.228	1.760	0.110	0.004
Ca	Co	Ti	Zr	Sn
0.001	0.025	0.004	0.004	0.009

The fabrication of the weld joint involves the initial root passes conducted by using SMAW and an automated multi-pass SAW process for the subsequent fill passes. The filler materials utilised were an E9015-B9 and an ER90S-B9 filler for the SMAW and the SAW processes, respectively. The fill passes were performed at a voltage of 30 V and an amperage of 400 A. Seventy-two weld beads were deposited as the electrode travelling at a speed of 381 mm/min. The Post Weld Heat Treatment (PWHT) was conducted at 732 °C for 2 hours.

Flat specimens were machined from the weld joint with a gauge length of 100 mm, a width of 60 mm, and a gauge thickness of 9 mm, Figure 1a. The gauge included the entire weld deposit with the fusion boundary at  $\sim 90^\circ$  to the stress loading direction. The high-temperature creep exposure of cross-weld specimens was carried out at 625 °C at a loading of uniaxial tension of 80 MPa. (EPRI: please add the details to indicate the locations used for the measurement of strain and strain rate) The creep testing was stopped at  $\sim 5,000$ ,  $\sim 8,000$  and  $\sim 11,000$  hours for detailed examinations of microstructure and creep damage.

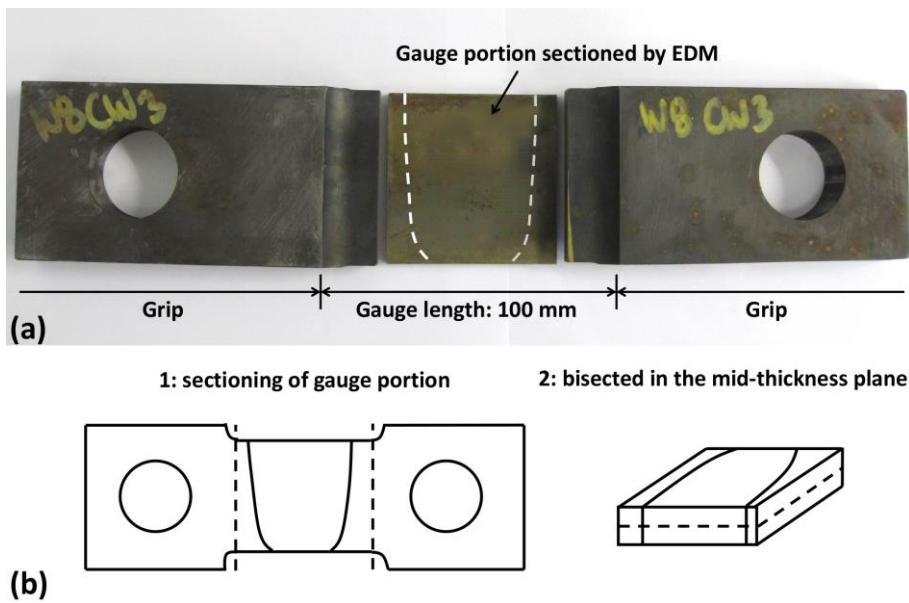


**Figure 1. (a) A picture showing a flat specimen containing the weld and the HAZ in the centre of gauge portion. The white dash lines indicate the location of fusion boundaries. (b) Schematic diagrams illustrating the sectioning of gauge position for detailed metallographic observations.**

## 2.2. Microstructural characterisation

The gauge portions were extracted from the cross-weld specimens and further bisected in the mid-thickness plane for microstructural examination after creep exposure, Figure 1b. The surfaces of gauge portions were prepared by using the standard metallographic preparation methods involved with grinding on SiC with water used as lubricant and polishing in the 3  $\mu\text{m}$  and 1  $\mu\text{m}$  diamond suspensions. A chemo-mechanical polishing

process was subsequently performed by using the 0.06  $\mu\text{m}$  colloidal silica suspension to achieve a surface finish suitable for EBSD analysis.

Hardness mapping was conducted by using a Struers Durascan 70 hardness testing system to identify the microstructural variation in the weld. The testing was carried out with a Vickers indenter operated at a test load of 0.2 kg with a uniform spacing of 0.1 mm. The testing condition used in the present research is consistent with the previous tests on the identical materials as detailed in [28]. Hardness mapping was carried out over an area of  $\sim 10 \times 5$  mm to ensure an accurate representation of the hardness in the weld metal, the HAZ regions, and the parent metal. The post analysis of the hardness data was performed by using the Origin software version 2020b.

A FEI Nova 600 Nanolab dual beam Focused Ion Beam (FIB)/Field Emission Gun (FEG)-SEM was used to characterise creep cavity, grain structure and secondary phase particles. An overview of the gauge portion was firstly achieved by using Backscattered Electron (BSE) imaging at an accelerating voltage of 10 kV. The BSE micrographs were collected sequentially over an area of  $\sim 60 \times 60$  mm at a pixel resolution of  $\sim 2$   $\mu\text{m}$  through the automated image acquisition capability of the FIB/FEG-SEM instrument. The BSE micrographs were then stitched to generate a large-scale montage by using the ImageJ software version 1.47t, providing an overview of the entire gauge portion. The quantitative analysis of creep cavity was carried out by using BSE imaging at a pixel resolution of  $\sim 0.2$   $\mu\text{m}$ . BSE micrographs were collected sequentially against the fusion boundary with a spacing of 0.25 mm with each covering an area of  $\sim 250 \times 200$   $\mu\text{m}$ . The number density and average size of the cavities were characterised by using a grey scale segmentation method utilising the ImageJ software. The minimum size of the cavities included for the analysis is  $\sim 0.5$   $\mu\text{m}$ . In addition, the distribution characteristics of the  $\text{Fe}_2(\text{W}, \text{Mo})$  Laves phases were investigated by using BSE imaging at the identical conditions utilised for cavity analysis. The quantitative analysis of Laves phases was carried out a grey scale segmentation method utilising the ImageJ software, with the minimum size (i.e. Feret's diameter) of the particles included for the analysis at  $\sim 0.5$   $\mu\text{m}$ . The secondary phase particles within creep cavities were investigated by using BSE imaging at an accelerating



voltage of 5 kV, with the quantitative analysis of these particles carried by using the ImageJ software. The chemical analysis of these particles was further performed by using Energy Dispersive X-ray (EDX) spectroscopy. This was conducted by using an Oxford Instruments® XmatS 80 SDD EDX system operated at an accelerating voltage of 10 kV to minimise the inferences from the surrounding matrix.

The quantitative analysis of grain structure was performed by using Electron Backscatter Diffraction (EBSD) with an EDAX Hikari XP camera at an accelerating voltage of 20 kV. Large-scale mapping of the matrix was carried out over an area of  $\sim 4 \times 1$  mm with a step size of 2  $\mu\text{m}$  to achieve an overview of the HAZ microstructure. The grain structure was further characterised in detail by using EBSD mapping at a step size of 0.1  $\mu\text{m}$  over an area of  $100 \times 50$   $\mu\text{m}$ . The post analysis of the EBSD data was conducted by using the TSL OIM analysis software version 7.2.1. The correlative analysis of the  $\text{M}_{23}\text{C}_6$  carbides particles was performed by using ion induced Secondary Electron (SE) imaging in the regions where the EBSD analyses were performed. The ion beam was operated at an accelerating voltage of 30 kV with a nominal beam current of 50 pA. A  $\text{XeF}_2$  gas flow was used to enhance the contrast differential between the  $\text{M}_{23}\text{C}_6$  carbides and the surrounding matrix [15,29]. The quantitative analysis of the  $\text{M}_{23}\text{C}_6$  carbides was then carried out by using a grey scale segmentation method to obtain their number density and average size (i.e. Feret's diameter) utilising the ImageJ software version 1.47t. The minimum size of the particles included for the analysis is  $\sim 50$  nm.

### **3. Results**

#### *3.1. Creep exposure*

The cross-weld specimens were exposed to high-temperature creep with a loading of uniaxial tension at 625 °C and 80 MPa. Figure 2 shows the creep strain and instantaneous creep rate versus time curves for the cross-weld specimens being tested up to  $\sim 11,000$  hours.

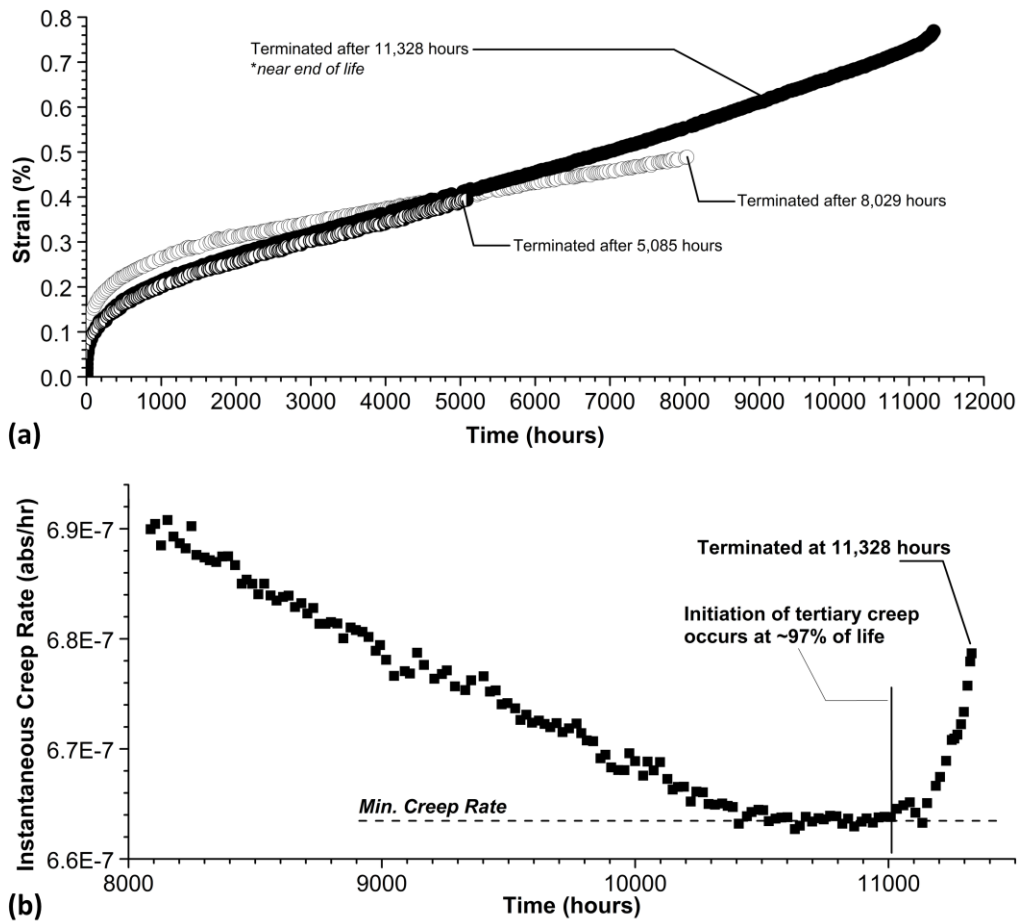
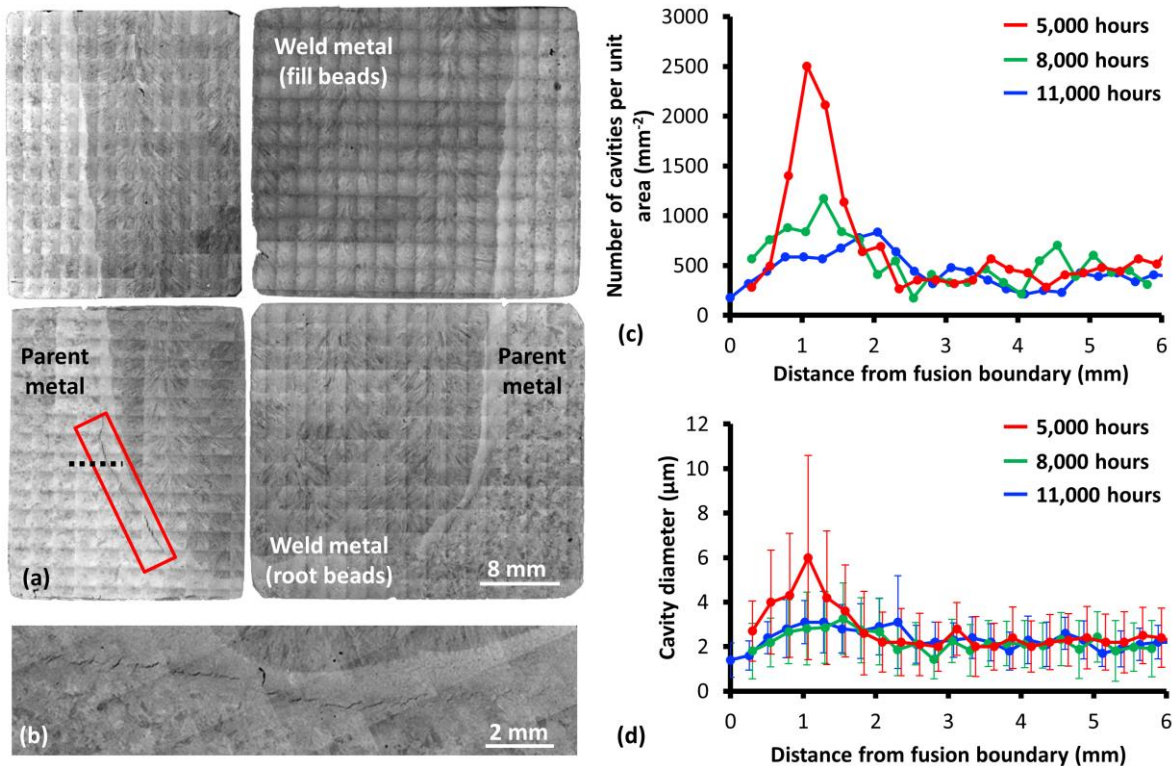


**Figure 2. Graphs showing the time dependent curves of (a) creep strain and (b) instantaneous creep rate for the cross-weld specimens tested up to ~ 5,000, ~ 8,000 and ~ 11,000 hours. Note: the reported strain values are averaged over an effective gauge length of 80 mm that includes the weld, both HAZs, and a portion of the base material on either side of the weld.**

Figure 2a shows that the longest test was stopped when the rupture of specimen was deemed imminent, whilst the tests terminated at ~ 5,000 and ~ 8,000 hours are within the stage of steady state creep. These tests were terminated at an estimated life fraction of ~ 50% (5,085 hours), ~ 80% (8,029 hours) and > 97% (11,328 hours) based on the experience with previous cross-weld testing on the 9% Cr tempered martensitic steels [30]. The minimum creep strain rate was reached at ~ 10,600 hours close to the onset of the tertiary creep stage, Figure 2b.

### 3.2. Microstructural overview and creep damage analysis

Overview of microstructure and creep damage distribution in cross-weld specimens was obtained by using BSE imaging. Figure 3 shows a large-scale montage of the BSE micrographs showing the entire gauge portion after ~ 11,000 hours of creep exposure together with the graphs presenting the number density and size of creep cavities across the HAZs after ~ 5,000, ~ 8,000 and ~ 11,000 hours of creep exposure.



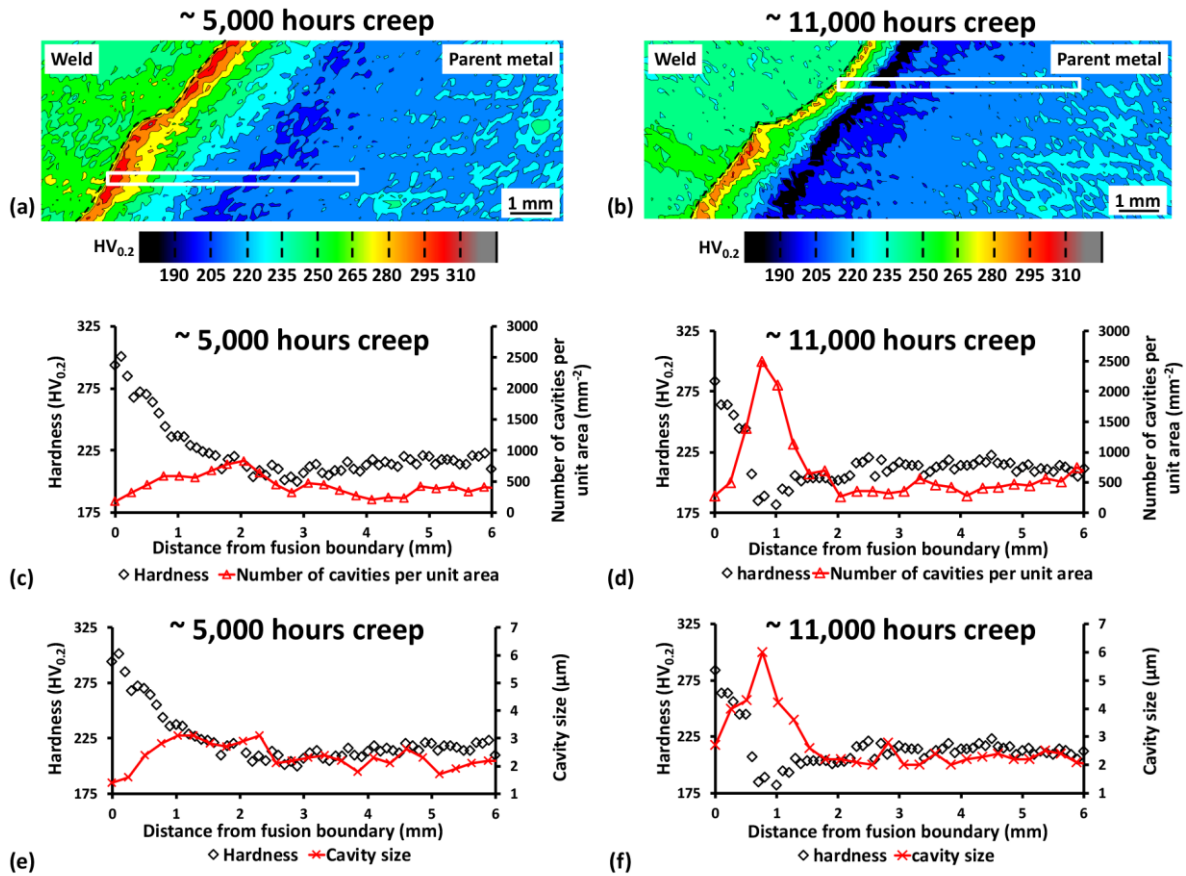
**Figure 3. (a) A large-scale montage of BSE micrographs showing the entire gauge portion after ~ 11,000 hours of creep exposure. The primary creep crack as indicated by the red box is detailed in (b). The graphs showing (c) the number per unit area and (d) the size of creep cavities after ~ 5,000, ~ 8,000 and ~ 11,000 hours of creep exposure are included to demonstrate the variation of creep cavities in the region as indicated by the dash line in (a). The lengths of error bars in (d) indicate the values of standard deviation.**

Figure 3a shows the primary creep damage present near the bottom of weld after ~ 11,000 hours of creep exposure. The crack is located at a distance of 1 – 2 mm away from the fusion boundary, Figure 3b. The number density and size of creep cavities are similar

between the specimens experiencing ~ 5,000 and ~ 8,000 hours of creep exposure, both showing slightly higher number density and larger size for the cavities 1 – 2 mm from the fusion boundary, Figures 3c and 3d. A higher level of creep damage in the HAZ suggests that cavities are preferentially formed from the early stage of creep before a life fraction of ~ 50% was reached. The similarity between the specimens with ~ 5,000 and ~ 8,000 hours of creep exposure further suggests that the number density of cavities has reached a saturated level and remains stable during the steady state regime. In the late stage of creep that are close to life end (i.e. > 95%), a higher number density and a larger size of defect-like features were observed in the local regions at 1 – 2 mm from the fusion boundary. This is due to the formation of plasticity induced micro-voids and the micro/macro-cracks that are formed via the link-up of cavities [12,31,32]. While the micro-voids and cracks are not the direct cause of creep rupture as they were formed in the very late stage of creep, the cavities that were formed in the early stage are expected to play an important role on creep failure.

### *3.3. Comparison between hardness and creep cavity*

The variation of hardness in the HAZ has been correlated with creep cavity. Figure 4 presents the hardness maps together with the graphs showing the trends of hardness and the variations in number density and size for the creep cavity within the HAZ.

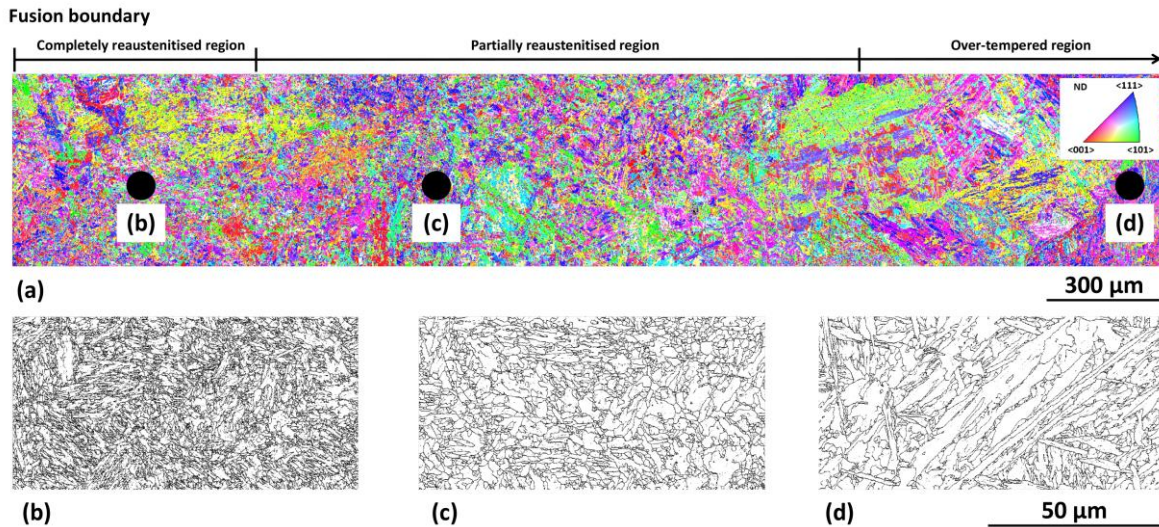


**Figure 4. Hardness maps showing the variation of hardness after (a) ~ 5,000 hours and (b) ~ 11,000 hours of creep exposure. The trends of hardness in the regions as indicated by white boxes are further compared with the variations of (c and d) number per unit area and (e and f) size of cavities.**

Figures 4a and 4b show that the hardness within the HAZ is in the range of 190 - 319 HV<sub>0.2</sub> and 176 - 282 HV<sub>0.2</sub> after ~ 5,000 hours and ~ 11,000 hours of creep exposure, respectively. The regions showing a higher level of creep damage are not correlated with the softest region and possess a hardness of 220 - 235 HV<sub>0.2</sub> in the specimen experiencing ~ 5,000 hours of creep exposure, Figures 4c and 4e. The location of peak damage is correlated with the regions showing the lowest hardness in the specimen with ~ 11,000 hours of creep exposure, Figures 4d and 4f.

### 3.4. Comparison between grain structure and creep cavity

The grain structure in the HAZ was analysed by using EBSD after ~ 11,000 hours of creep exposure. Figure 5 shows an EBSD overview of grain structure in the HAZ together with the maps detailing the characteristics of grain structure.



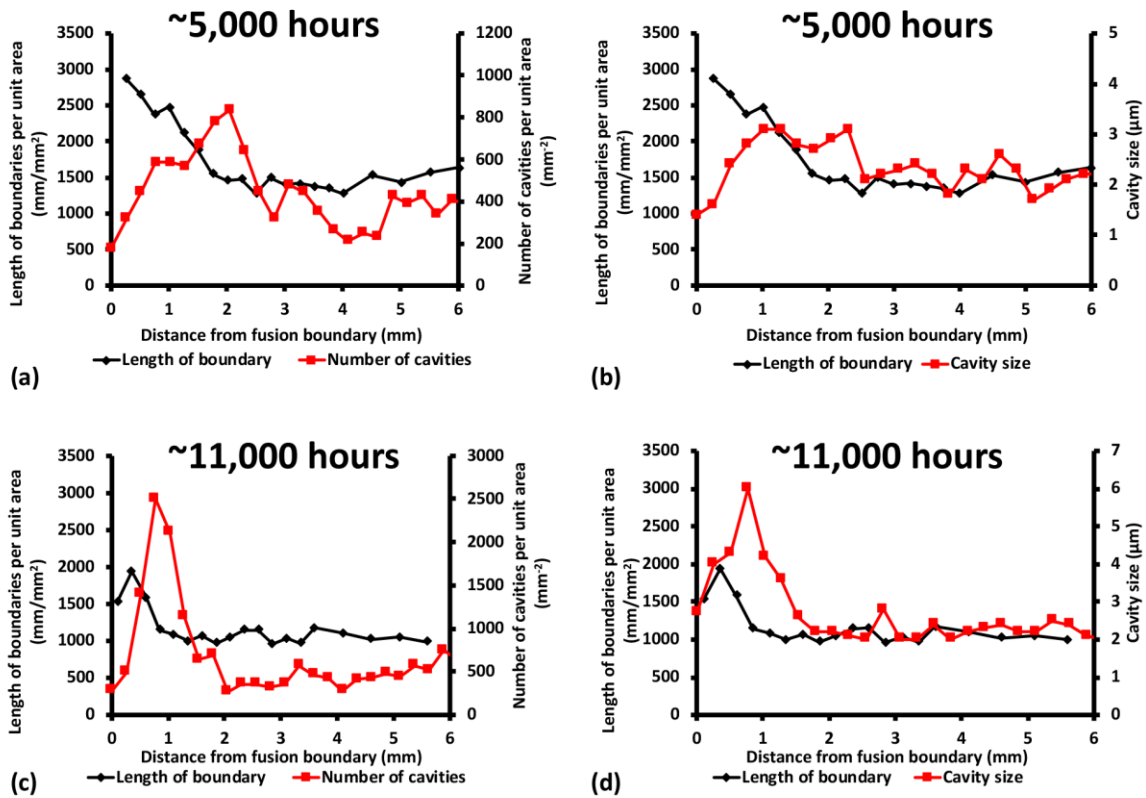
**Figure 5. (a) An EBSD orientation map showing the overall gradient of grain structure in the HAZ. EBSD grain boundary maps were also obtained from the regions as labelled in (a) to provide details of grain boundary ( $> 2^\circ$ ) at (b) 0.3 mm (CTZ), (c) 1.0 mm (PTZ), (d) 3.0 mm (OTZ) from the fusion boundary.**

Figure 5a shows that the HAZ is within a distance of 3 mm from the fusion boundary. The grain structure within the HAZ is more refined as compared to the parent metal, which is consistent with the previous observations in the HAZ of Grade 92 steel welds prior to creep [15,27]. Figure 5b shows a refined grain structure composed of the grains  $< 10 \mu\text{m}$  in length in the region  $\sim 0.3 \text{ mm}$  from the fusion boundary, whilst a duplex grain structure composed of the coarser lath-like grains  $10 - 15 \mu\text{m}$  in length and the smaller grains  $< 3 \mu\text{m}$  in diameter was observed in the region  $\sim 1.0 \text{ mm}$  from the fusion boundary, Figure 5c. The martensitic matrix in the region at  $\sim 3 \text{ mm}$  from the fusion boundary is considerably coarser and predominantly composed of the lath-like grains  $> 15 \mu\text{m}$  in length and  $> 2 \mu\text{m}$  in width, Figure 5d. Based on the general trend of microstructure as detailed in Figure 5a, it is proposed that the HAZ is classified based on the observation from the initial weld HAZ as

277 detailed in the previous studies [15,27]. The grain structure in the regions  $< 0.5$  mm from  
278 the fusion boundary is similar to the microstructure as produced after thermal cycles with a  
279 peak temperature above the  $Ac_3$  temperature. In addition, the duplex microstructure in the  
280 regions at  $0.5 - 2.5$  mm from the fusion boundary evidences the partial re-austenitisation  
281 arising from the experience to thermal cycles with a peak temperature between the  $Ac_1$  and  
282 the  $Ac_3$  temperatures during welding. The microstructure at  $> 2.5$  mm from the fusion  
283 boundary is not significantly varied from the original microstructure of the parent metal  
284 upon the experience to thermal cycles with peak temperatures below the  $Ac_1$  temperature.

285 Creep cavities are further compared with the characteristics of grain boundary in the HAZ.  
286 Figure 6 presents the graphs showing the variation of creep cavity and the length density of  
287 grain boundary against the distance from fusion boundary. The length density of grain  
288 boundary is decreased in the HAZ against the distance from fusion boundary after  $\sim 5,000$   
289 and  $\sim 11,000$  hours of creep exposure. It is clear that the regions with the most significant  
290 creep damage are not correlated with the peak of grain boundary density in the CTZ  
291 regions.





**Figure 6.** Graphs comparing the length density of grain boundary ( $> 2^\circ$ ) with (a and c) the number per unit area and (b and d) the size of cavities after (a and b) ~ 5,000 hours and (c and d) ~ 11,000 hours of creep exposure.

### 3.5. Comparison between the $M_{23}C_6$ carbides and creep cavity

The  $M_{23}C_6$  carbides across the HAZ were analysed by using ion induced SE imaging.

Figure 7 presents the micrographs showing the precipitate particles in the HAZ after ~ 11,000 hours of creep exposure. The number per unit area and size of the  $M_{23}C_6$  carbides were quantitatively analysed, with the results presented in Table 2.



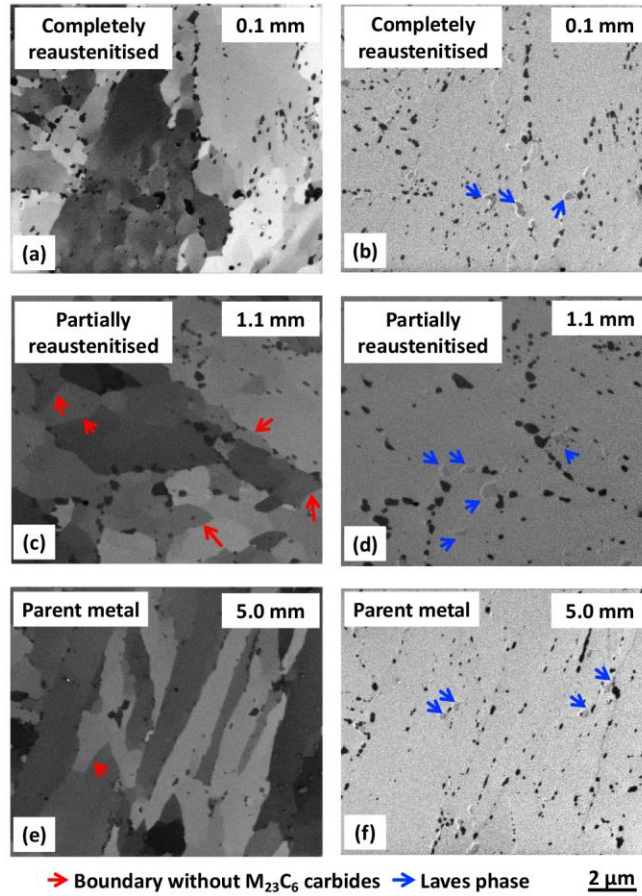


**Figure 7.** Ion induced SE micrographs showing the M<sub>23</sub>C<sub>6</sub> carbides in (a, b) the CTZ, (c, d) the PTZ and (e, f) the parent metal after ~ 11,000 hours of creep exposure. The micrographs were collected from the regions at (a and b) 0.1 mm, (c and d) 1.1 mm and (e and f) 5.0 mm from the fusion boundary. The micrographs as shown in (a, c, e) were collected without XeF<sub>2</sub> gas to visualise grain structure, whilst (b, d, f) were collected with a XeF<sub>2</sub> gas flow to enhance the contrast of the M<sub>23</sub>C<sub>6</sub> carbides. The arrows indicate the grain boundaries where the particles are absent and the Laves phases appearing light grey.

**Table 2.** The number per unit area and mean size of the M<sub>23</sub>C<sub>6</sub> carbides in the regions at 0.1 mm, 1.1 mm and 5.0 mm from the fusion boundary. Five micrographs were collected from each region, covering a total area of ~ 600 μm<sup>2</sup>.

Distance from the fusion line (mm)	0.1	1.1	5.0
Number of particles per unit area (mm <sup>-2</sup> )	1,761,364	845,170	1,534,091
Size of particles (μm)	0.18 ± 0.10	0.23 ± 0.22	0.17 ± 0.14

The ion induced SE micrographs collected at different conditions facilitate a direct correlation between grain structure and the M<sub>23</sub>C<sub>6</sub> carbides appearing dark grey [15,29].

Figures 7a, 7b, 7e and 7f show that the grain boundaries in the martensitic microstructure are effectively stabilised by the carbide particles in the regions at 0.1 mm and 5.0 mm from fusion boundary. However, a lack of precipitate particles on the boundaries were observed in the HAZ region at 1.1 mm from the fusion boundary, Figures 7c and 7d. This region is correlated with the location of peak damage present in the HAZ after ~ 11,000 hours of creep exposure. In particular, the precipitate particles at 1.1 mm from the fusion boundary are evidently larger in size and lower in number density. This has been confirmed by the results of quantitative analysis as presented in Table 2. The coarser precipitate particles are present due to the partial dissolution of the pre-existing carbides in the original microstructure during welding, followed by coarsening to large particles during the subsequent PWHT and creep testing [5,6]. The retained  $M_{23}C_6$  carbides also hinder the formation of precipitates during PWHT and creep testing, leading to a lower number density of carbides in the local regions.

The distribution of the  $M_{23}C_6$  carbides on grain boundaries has been evaluated by normalising the number density of carbides by using the length density of boundaries. Figure 8 compares the trend of creep cavity to the variation of carbide distribution as a function of the distance from fusion boundary.

Figure 8 shows that the normalised number density of the  $M_{23}C_6$  carbides is considerably lower in the HAZ as compared to the parent metal due to the refinement of grain structure. In addition, the regions with larger cavity sizes are correlated with a lower number density of carbides in both the specimens experiencing ~ 5,000 and ~ 11,000 hours of creep exposure. The location of peak damage is also correlated with the regions showing the lowest number density of carbides after ~ 11,000 hours of creep exposure, Figure 8b.

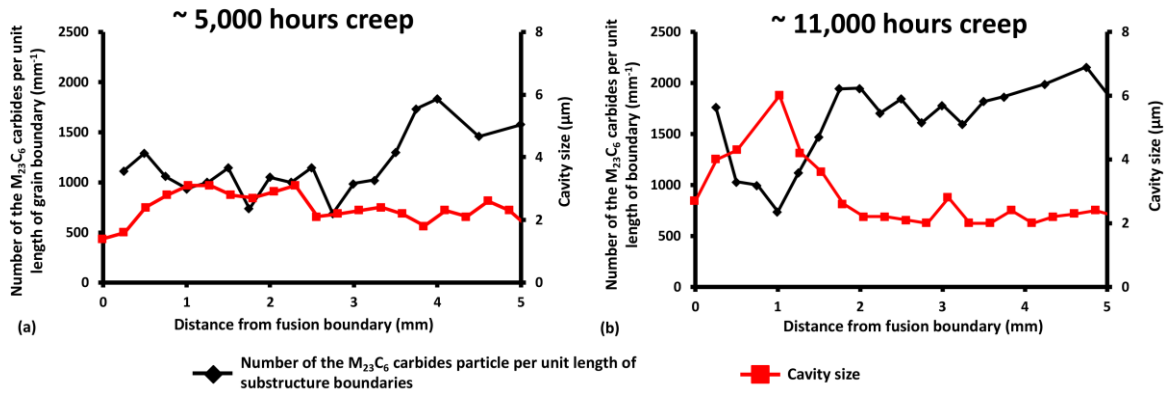


**Figure 8.** The graphs comparing the trend of cavity size to the number density of the  $M_{23}C_6$  carbides per unit length of grain boundary ( $> 2^\circ$ ) after (a)  $\sim 5,000$  and (b)  $\sim 11,000$  hours of creep exposure.

### 3.6. Comparison between the Laves phase and creep cavity

Figure 9 presents the BSE micrographs showing the Laves phases within the HAZ and the parent metal after  $\sim 11,000$  hours of creep exposure. The quantitative analysis for the number density and size of these phases was also conducted with the results presented in Table 3.

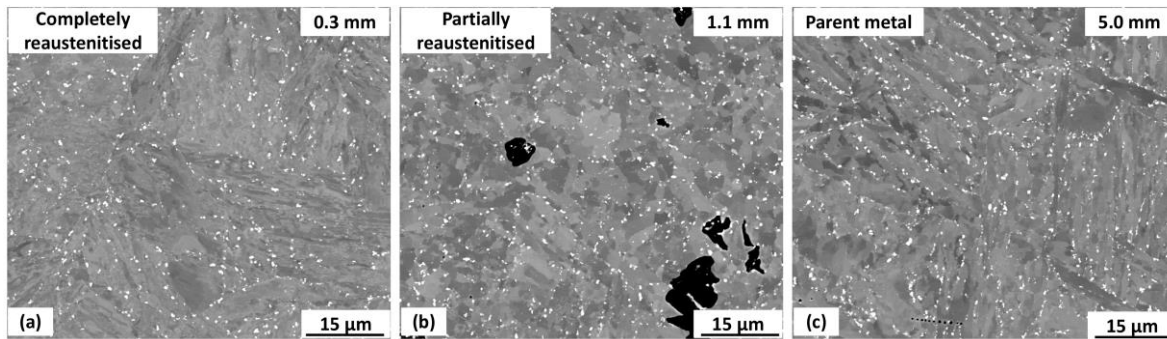


**Figure 9.** BSE micrographs showing the Laves phases (bright particles) in the regions at (a) 0.1 mm, (b) 1.1 mm and (c) 5.0 mm from the fusion boundary after  $\sim 11,000$  hours of creep exposure.

**Table 3.** The number per unit area and mean size of the Laves phases at 0.1 mm, 1.1 mm and 5.0 mm from the fusion boundary after  $\sim 11,000$  hours of creep exposure. Five micrographs were collected from each region, covering a total area of  $\sim 10,000 \mu m^2$ .

Distance from the fusion boundary (mm)	0.1	1.1	5.0
Number of particles ( $mm^{-2}$ )	321,070	361,080	330,682

Size of particles ( $\mu\text{m}$ )	$0.44\pm0.23$	$0.38\pm0.24$	$0.44\pm0.24$
-------------------------------------	---------------	---------------	---------------

Figure 9 shows the Laves phases appearing shiny bright in the BSE micrographs due to the abundance of heavy elements such as W and Mo [33]. These phases are preferentially distributed on grain boundaries. Table 3 shows that the number density of the Laves phases is not significantly varied between the HAZ and the parent metal. The number density at 1.1 mm from fusion boundary is slightly higher as compared to the regions at 0.1 and 5.0 mm, whilst the average size is slightly smaller. The increased number density of Laves phase is linked with a higher length density of grain boundary, particularly the high angle boundary of austenitic grains. This has been evidenced in the previous studies that demonstrate a higher length density of austenitic grain boundaries upon partial reaustenitisation during welding [15,27]. The slightly smaller size of Laves phases in the local regions is attributable to the retained  $\text{M}_{23}\text{C}_6$  carbides being remained after incomplete dissolution during welding. The presence of these particles is expected to cause a lower content of W and Mo in solid solution and, in turn, hinder the formation of Laves phases.

#### *Cavity association with $\text{Al}_2\text{O}_3$ , MnS and BN phases*

Figure 10 shows the  $\text{Al}_2\text{O}_3$ , MnS and BN phases in the HAZ after  $\sim 11,000$  hours of creep exposure together with the EDX spectra confirming their chemical compositions. A close association between creep cavities and the  $\text{Al}_2\text{O}_3$ , MnS and BN phases has been confirmed after  $\sim 11,000$  hours of creep exposure. In addition, the distribution characteristics of these particles were quantitatively measured by using BSE imaging for a comparison between the HAZ and the parent metal, Table 4. The quantitative analysis shows that the number density and mean size of the  $\text{Al}_2\text{O}_3$ , MnS and BN phase particles are not significantly varied between regions of the HAZ and the parent metal at  $\sim 1.0$  and  $\sim 5.0$  mm from the fusion boundary, respectively.

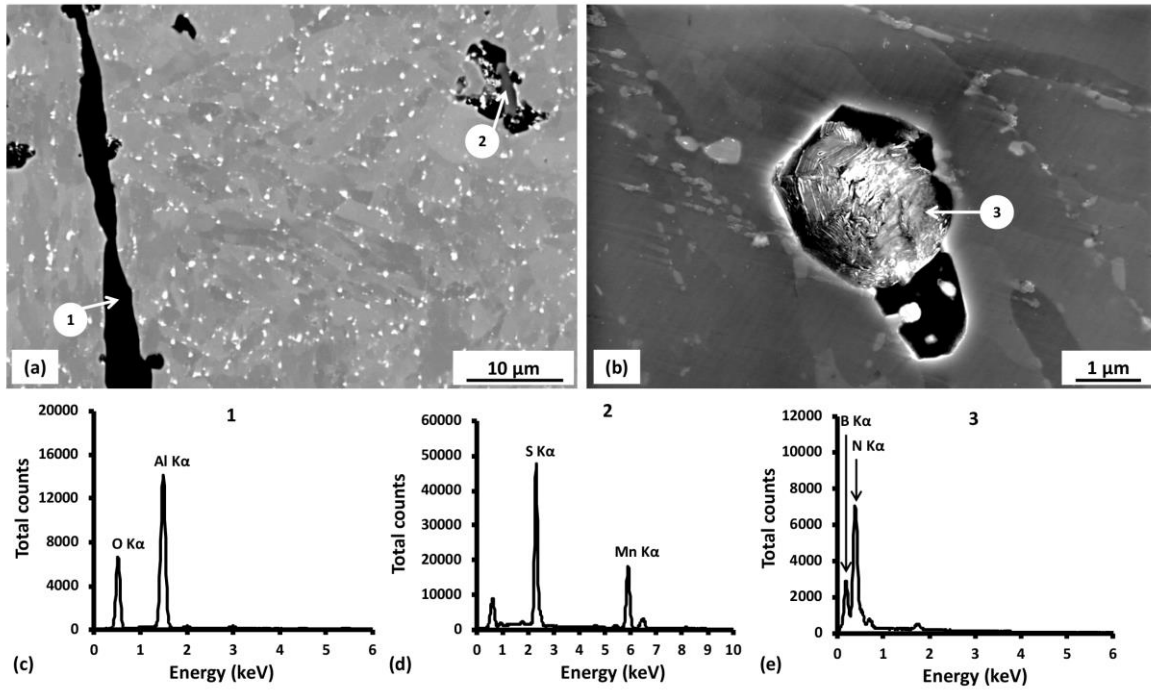


**Figure 10.** Micrographs showing the (a)  $\text{Al}_2\text{O}_3$  and MnS particles and (b) BN phases within the cavities after  $\sim 11,000$  hours of creep exposure. The EDX spectra collected from these particles are shown in (c – e).

**Table 4.** The number per unit area and mean size of the  $\text{Al}_2\text{O}_3$ , MnS and BN particles at 1.1 mm and 5.0 mm from the fusion boundary after  $\sim 11,000$  hours of creep exposure. Five BSE micrographs were collected from each region, covering a total area of  $\sim 200,000 \mu\text{m}^2$ .

Distance from the fusion boundary (mm)	1.0	5.0
Number of particles per unit area ( $\text{mm}^{-2}$ )	$908 \pm 249$	$1090 \pm 165$
Size of particles ( $\mu\text{m}$ )	$0.97 \pm 0.23$	$0.83 \pm 0.17$

## 4. Discussion

### 4.1. Definition of damage susceptible region in the HAZ

In comparison to the existing method used to categorise the general trend of microstructure in the HAZ of steel welds [4,5], the previous studies have proposed a more accurate description of the HAZ for the specific case of Grade 92 steel, as detailed in [15,27]. Figure 11a shows the microstructure in the HAZ of a single-pass weld as divided into three distinct regions based on the characteristics of grain structure and secondary precipitate phases, i.e.,

the CTZ, the PTZ and the OTZ, [15]. Figure 11b further demonstrates a more complicated case where there is an accumulated effect on microstructure arising from the multiple experiences of thermal cycle as in a multi-pass weld [27].

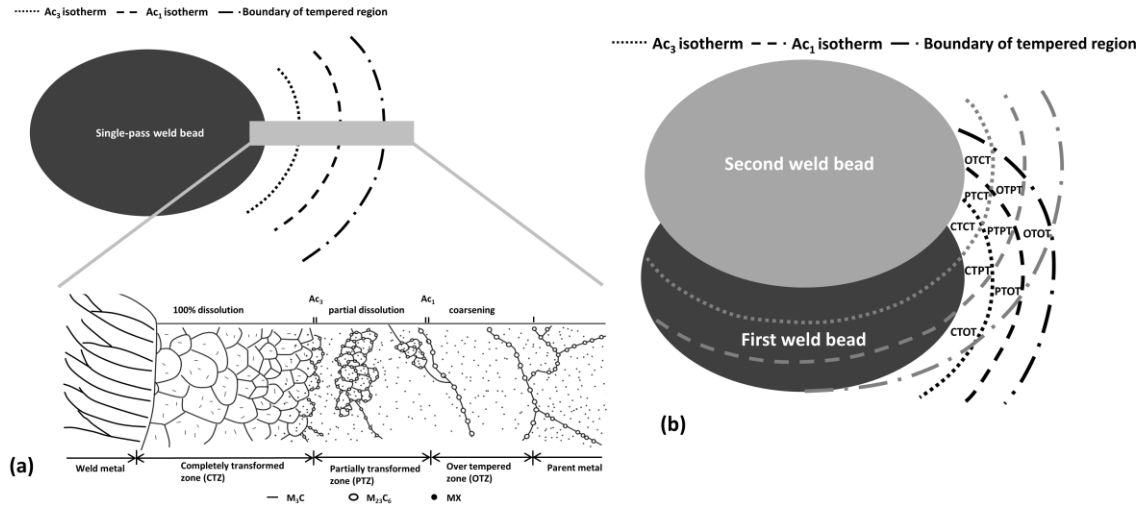


**Figure 11. Schematic diagrams summarising the classification of the microstructures within the HAZs of (a) single-pass and (b) double-/multi-pass welds constructed by using Grade 92 steel as proposed in the previous studies [15,27]. The HAZ of a single-pass weld is divided into the Completely Transformed zone (CTZ), Partially Transformed Zone (PTZ) and Over-Tempered Zone (OTZ), which experience the thermal cycle with peak temperatures  $> Ac_3$ , between  $Ac_1$  and  $Ac_3$  and  $< Ac_1$  temperatures, respectively. The HAZ of a double-/multi-pass weld is further classified by using the same designations to indicate the regions where the regions of CTZ, PTZ and OTZ are overlapped. For instance, ‘CTCT’ indicates the regions that experience two thermal cycles with peak temperatures both above the  $Ac_3$  temperature during welding.**

As demonstrated in the HAZ of a multi-pass weld [27], thermal experiences with a peak temperature above the  $Ac_3$  temperature lead to complete dissolution of the pre-existing secondary precipitates in a completely reaustenitised matrix as in the regions of CTCT, CTPT, CTOT, PTCT and OTCT, Figure 11b. The resultant microstructures in these regions are composed of the austenitic grains typically  $\sim 50 \mu m$  in size with no coarse particles observed. The microstructure in the regions of PTPT, PTOT and OTPT contains coarse particles of the retained secondary precipitates that were not completely dissolved after experiencing the thermal cycles with peak temperatures between the  $Ac_1$  and the  $Ac_3$

temperatures [27]. The matrix in these regions varies from a refined, completely reaustenitised grain structure to a duplexed microstructure containing coarse lath-like grains as peak temperatures of weld thermal cycles decrease from the  $Ac_3$  to the  $Ac_1$  temperatures. The microstructure in the regions of OTOT is not significantly varied from the parent metal, while the hardness is lower and secondary precipitates are slightly coarsened [27]. In comparison to the observations from the present study, it is clear that creep cavitation was preferentially occurred in the regions experiencing thermal cycles with the inter-critical peak temperatures between the  $Ac_1$  and the  $Ac_3$  temperatures, e.g. the regions of PTPT, PTOT and OTPT. This is evidenced by the observation of coarse  $M_{23}C_6$  carbides particles in combination with a refined/duplexed grain structure, Figures 5 and 7.

Comparing with the existing studies on Grade 91 and Grade 92 steel welds, the reported locations of creep rupture coincides with the regions showing the highest extent of creep damage as presented in the current study. For instance, creep rupture is reported to take place in the FG-HAZ region in Grade 92 steel welds as tested at 650°C with a stress level of < 120 MPa [34,35]. Grade 91 steel welds are also ruptured at similar locations as tested at 650°C in a stress range of 40 – 80 MPa [36]. In these cases, coarse particles of secondary precipitate in the matrix showing a refined grain structure were observed in the local regions close to rupture surface (e.g. [36]). Following the conventional definition of the HAZ in steel welds, it was hypothesized that the reported locations of creep rupture are within the regions experiencing the thermal cycles with peak temperatures above the  $Ac_3$  temperature [4,5]. In the present case, the post-mortem analysis in the HAZ facilitates an unambiguous link between the location of creep rupture and the initial microstructure in the as-fabricated state, and further, the history of thermal experiences during welding. As discussed above, the location of creep rupture has been confirmed in the regions experiencing the thermal cycles with peak temperatures below the  $Ac_3$  and above the  $Ac_1$  temperatures.

#### *4.2. microstructural influence on creep cavitation*

To investigate the influence of microstructure on creep cavitation, the distribution of creep cavity has been compared to the variation of microstructure in the HAZ. Table 5 summarises the overall gradient of microstructure as a function of the distance from fusion boundary and the correlation between microstructure and creep damage.

**Table 5. A summary of the microstructural factors that have been correlated with the distribution of creep damage.**

Microstructural property	Figure number	Observations
Hardness	4	1. Preferential creep cavity is not occurred in the softest region after ~ 5,000 hours of creep exposure; 2. The location of peak damage is correlated with the lowest hardness after ~ 11,000 hours of creep exposure.
Grain structure	5, 6	Preferential creep cavity is not occurred in the region possessing the highest length density of grain boundary.
M <sub>23</sub> C <sub>6</sub> carbides	7, 8	The regions showing a higher level of creep damage are correlated with a lower number density of carbides both after ~ 5,000 and ~ 11,000 hours of creep exposure.
Laves phase	9	No significant variation between the HAZ and the parent metal.
Al <sub>2</sub> O <sub>3</sub> , MnS, BN	10	Close association with cavities after ~ 11,000 hours of creep exposure;

The comparison between microstructure and creep cavity shows that cavitation is not necessarily occurred in the regions with a lower hardness or a higher level of grain boundary density, Table 5. This is consistent with the observations from previous studies showing that preferential creep cavitation is not occurred in the regions with lower hardness or higher boundary density [5,23–26]. The lower hardness measured from the location of peak damage after 11,000 hours of creep exposure is caused by the presence of concentrated creep damage in the local regions.

An inhomogeneous distribution of the M<sub>23</sub>C<sub>6</sub> carbides on lath and grain boundaries was observed in the local regions due to incomplete dissolution of the pre-existing particles during welding [15,27]. This is consistent with the observations from similar materials as previously detailed in [6,37]. It is known that the major contribution of the M<sub>23</sub>C<sub>6</sub> carbides to creep resistance is increasing the stability of microstructure through a particle pinning effect [1,38]. In this case, the lack of carbides on grain boundary and the coarsening of precipitates during creep have a deleterious effect on creep strength in the local regions



[39–41]. This is further related to concentrated cavitation due to strain localisation at an unfavourable stress state upon mechanical constraints from the adjacent regions in the HAZ and the parent metal that possess a higher creep strength [11,25].

The Laves phase particles that are grown above a critical size are related to the premature creep failure in the HAZ [42]. The Laves phase particles that are large in size normally act as the preferred sites for cavity nucleation. In addition, the Laves phases consuming W and Mo deteriorate their effect of solid solution strengthening for the martensitic matrix [43]. However, in this case, the Laves phases are relatively smaller in size and higher in number density as appeared in the regions showing a higher extent of creep cavitation. This suggests that these phases are not directly linked with the preferential cavitation in the PTZ.

Importantly, creep cavities are closely associated with the  $\text{Al}_2\text{O}_3$ , MnS and BN phases after ~ 11,000 hours of creep exposure. This observation is consistent with the existing studies on 9% Cr steels as previously detailed in [21,44]. The large secondary phase particles above a critical size are known as the preferred sites for cavity nucleation in 9% Cr steels [21,30,44]. In particular, a recent study on Grade 92 steel welds reveals a close association between creep cavities and BN particles from a life fraction of < 50% to the stage close to life end at a fraction of > 95% [22]. Detailed metallographic observations further reveal that cavities were initiated via the link-up of micro-pores/defects presented on BN interfaces from the initial as-fabricated condition prior to creep [22]. During creep, the cavities are developed to larger sizes as present in the PTZ and, in turn, contribute to creep rupture in the HAZ. This is related to a higher extent of interfacial decohesion on the BNs in the PTZ that promotes the formation of cavities [22]. This further explains the observation of a higher extent of creep cavitation in the PTZ (Figure 3), while the number density and size of the  $\text{Al}_2\text{O}_3$ , MnS and BN particles are not significantly varied between HAZ and parent metal (Table 4).

## **5. Conclusions**

In the present study, preferential creep cavitation was observed in the HAZ of a multi-pass 9% Cr steel weld after high temperature creep exposure. A systematic comparison between

creep cavity and HAZ microstructure has revealed a high susceptibility to creep cavitation in the microstructures composed of refined grains in combination with a sub-optimal distribution of the  $M_{23}C_6$  carbides. However, the regions showing concentrated creep damage are not correlated with the regions showing the lowest hardness or the most refined grain structure. Creep cavities are nucleated on the large secondary phase particles such as  $Al_2O_3$ , MnS and BN. The local high density of creep cavities in the HAZ is thus a consequence of strain localisation in the microstructures with low creep strength and large secondary phase particles. The HAZ microstructures that are highly susceptible to creep cavitation are generated upon thermal exposure with the peak temperatures between the  $Ac_1$  and the  $Ac_3$  transus temperatures during welding. Therefore, it is vital that alloy composition, thermo-mechanical practices and final heat treatment are controlled to produce weldments with optimal microstructures for an enhanced creep strength in the HAZ.

## **Acknowledgement**

This work was supported by the Electric Power Research Institute, Palo Alto, California, USA. The authors gratefully acknowledge Dr Geoff West (WMG, Warwick University, UK) for valuable contributions. The authors also acknowledge use of facilities within the Loughborough Materials Characterisation Centre (LMCC).

## **Data availability**

The raw data supporting the findings are available from the corresponding authors of this study.

## **References**

- [1] P.J. Ennis, A. Czyrska-Filemonowicz, Recent advances in creep-resistant steels for power plant applications, *Sadhana*. 28 (2003) 709–730.
- [2] G.M. Marcello Consonni, Review of current practice for welding of Grade 92 steel,

512 Weld. Cut. 11 (2013) 169–173.

513 [3] H. Rampaul, Pipe welding procedures, Industrial Press, New York, 2003.

514 [4] D.J. Abson, J.S. Rothwell, Review of type IV cracking of weldments in 9-12% Cr  
515 creep strength enhanced ferritic steels, *Int. Mater. Rev.* 58 (2013) 437–473.

516 [5] J.A. Francis, W. Mazur, H. Bhadeshia, Review type IV cracking in ferritic power  
517 plant steels, *Mater. Sci. Technol.* 22 (2006) 1387–1395.

518 [6] Y. Liu, S. Tsukamoto, T. Shirane, F. Abe, Formation mechanism of Type IV failure  
519 in high Cr ferritic heat-resistant steel-welded joint, *Metall. Mater. Trans. A.* 44  
520 (2013) 4626–4633.

521 [7] S.K. Albert, M. Matsui, T. Watanabe, H. Hongo, K. Kubo, M. Tabuchi, Variation in  
522 the Type IV cracking behaviour of a high Cr steel weld with post weld heat  
523 treatment, *Int. J. Press. Vessel. Pip.* 80 (2003) 405–413.

524 [8] F. Masuyama, M. Matsui, N. Komai, Creep rupture behavior of advanced 9-12% Cr  
525 steel weldment, *Key Eng. Mater.* 171 (1999) 99–108.

526 [9] T. Sakthivel, M. Vasudevan, K. Laha, P. Parameswaran, K.S. Chandravathi, S.P.  
527 Selvi, V. Maduraimuthu, M.D. Mathew, Creep rupture behavior of 9Cr–1.8 W–0.5  
528 Mo–VNb (ASME grade 92) ferritic steel weld joint, *Mater. Sci. Eng. A.* 591 (2014)  
529 111–120.

530 [10] J.S. Lee, K. Maruyama, Mechanism of microstructural deterioration preceding type  
531 IV failure in weldment of mod. 9Cr-1Mo steel, *Met. Mater. Int.* 21 (2015) 639–645.

532 [11] K. Shinozaki, D. Li, H. Kuroki, H. Harada, K. Ohishi, T. Sato, Observation of type  
533 IV cracking in welded joints of high chromium ferritic heat resistant steels, *Sci.*  
534 *Technol. Weld. Join.* 8 (2003) 289–295.

535 [12] M.E. Kassner, T.A. Hayes, Creep cavitation in metals, *Int. J. Plast.* 19 (2003) 1715–  
536 1748.

- 537 [13] K. Laha, K.S. Chandravathi, P. Parameswaran, K.B.S. Rao, S.L. Mannan,  
538 Characterization of microstructures across the heat-affected zone of the modified  
539 9Cr-1Mo weld joint to understand its role in promoting Type IV cracking, Metall.  
540 Mater. Trans. A. 38 (2007) 58–68.
- 541 [14] Y. Wang, R. Kannan, L. Li, Characterization of as-welded microstructure of heat-  
542 affected zone in modified 9Cr–1Mo–V–Nb steel weldment, Mater. Charact. 118  
543 (2016) 225–234.
- 544 [15] X. Xu, G.D. West, J.A. Siefert, J.D. Parker, R.C. Thomson, The influence of thermal  
545 cycles on the microstructure of Grade 92 steel, Metall. Mater. Trans. A. 48 (2017)  
546 5396–5414.
- 547 [16] S.B. Wang, X.F. Chang, J. Key, New insight into high-temperature creep  
548 deformation and fracture of T92 steel involving precipitates, dislocations and  
549 nanovoids, Mater. Charact. 127 (2017) 1–11.
- 550 [17] J. Hald, Microstructure and long-term creep properties of 9–12% Cr steels, Int. J.  
551 Press. Vessel. Pip. 85 (2008) 30–37.
- 552 [18] F. Abe, H. Araki, T. Noda, The effect of tungsten on dislocation recovery and  
553 precipitation behavior of low-activation martensitic 9Cr steels, Metall. Trans. A. 22  
554 (1991) 2225–2235.
- 555 [19] D. Li, K. Shinozaki, H. Harada, K. Ohishi, Investigation of precipitation behavior in  
556 a weld deposit of 11Cr-2W ferritic steel, Metall. Mater. Trans. A. 36 (2005) 107–  
557 115.
- 558 [20] K. Sakuraya, H. Okada, F. Abe, BN type inclusions formed in high Cr ferritic heat  
559 resistant steel, Energy Mater. (2013).
- 560 [21] Y. Gu, G.D. West, R.C. Thomson, J. Parker, Investigation of creep damage and  
561 cavitation mechanisms in P92 steels, in: Adv. Mater. Technol. Foss. Power Plants -  
562 Proc. from 7th Int. Conf., ASM International, 2014: pp. 596–606.

- 563 [22] X. Xu, J.A. Siefert, J.D. Parker, R.C. Thomson, Localised creep cavitation on boron  
564 nitride in the heat affected zone of 9% Cr tempered martensitic steel welds, Mater.  
565 Des. 196 (2020) 109046.
- 566 [23] M. Tabuchi, T. Watanabe, K. Kubo, M. Matsui, J. Kinugawa, F. Abe, Creep crack  
567 growth behavior in the HAZ of weldments of W containing high Cr steel, Int. J.  
568 Press. Vessel. Pip. 78 (2001) 779–784.
- 569 [24] F. Abe, M. Tabuchi, M. Kondo, S. Tsukamoto, Suppression of Type IV fracture and  
570 improvement of creep strength of 9Cr steel welded joints by boron addition, Int. J.  
571 Press. Vessel. Pip. 84 (2007) 44–52.
- 572 [25] H. Hongo, M. Tabuchi, T. Watanabe, Type IV creep damage behavior in Gr. 91 steel  
573 welded joints, Metall. Mater. Trans. A. 43 (2012) 1163–1173.
- 574 [26] K. Kimura, Y. Takahashi, Evaluation of long-term creep strength of ASME Grades  
575 91, 92, and 122 type steels, in: ASME 2012 Press. Vessel. Pip. Conf., American  
576 Society of Mechanical Engineers, 2012: pp. 309–316.
- 577 [27] X. Xu, G.D. West, J.A. Siefert, J.D. Parker, R.C. Thomson, Microstructural  
578 Characterization of the heat-affected zones in Grade 92 steel welds: double-pass and  
579 multipass welds, Metall. Mater. Trans. A. 49 (2018) 1211–1230.
- 580 [28] J.A. Siefert, J.P. Shingledecker, J.D. Parker, Optimization of vickers hardness  
581 parameters for micro-and macro-indentation of Grade 91 steel, J. Test. Eval. 41  
582 (2013) 1–10.
- 583 [29] L. Li, R. MacLachlan, M. A. E. Jepson, R. Thomson, Microstructural evolution of  
584 boron nitride particles in advanced 9Cr Power plant steels, Metall. Mater. Trans. A.  
585 44 (2013) 3411–3418.
- 586 [30] J. Parker, Factors affecting Type IV creep damage in Grade 91 steel welds, Mater.  
587 Sci. Eng. A. 578 (2013) 430–437.
- 588 [31] F. Abe, T.U. Kern, R. Viswanathan, Creep-resistant steels, Woodhead Pub., 2008.

- 589 [32] J. Lin, Y. Liu, T.A. Dean, A review on damage mechanisms, models and calibration  
590 methods under various deformation conditions, *Int. J. Damage Mech.* 14 (2005)  
591 299–319.
- 592 [33] O. Prat, J. Garcia, D. Rojas, G. Sauthoff, G. Inden, The role of Laves phase on  
593 microstructure evolution and creep strength of novel 9% Cr heat resistant steels,  
594 *Intermetallics*. 32 (2013) 362–372.
- 595 [34] L. Falat, A. Výrostková, V. Homolová, M. Svoboda, Creep deformation and failure  
596 of E911/E911 and P92/P92 similar weld-joints, *Eng. Fail. Anal.* 16 (2009) 2114–  
597 2120.
- 598 [35] W. Xue, P. Qian-gang, L. Zhi-jun, Z. Hui-qiang, T. Yong-shun, Creep rupture  
599 behaviour of P92 steel weldment, *Eng. Fail. Anal.* 18 (2011) 186–191.
- 600 [36] T. Watanabe, M. Tabuchi, M. Yamazaki, H. Hongo, T. Tanabe, Creep damage  
601 evaluation of 9Cr–1Mo–V–Nb steel welded joints showing Type IV fracture, *Int. J.*  
602 *Press. Vessel. Pip.* 83 (2006) 63–71.
- 603 [37] R.C. MacLachlan Sanchez-Hanton, J.J., Thomson. R.C., The effect of simulated post  
604 weld heat treatment temperature overshoot on microstructural evolution in P91 and  
605 P92 power plant steels, in: *Adv. Mater. Technol. Foss. Power Plants - Proc. from 6th*  
606 *Int. Conf., ASM International*, 2011: 787–799.
- 607 [38] K. Maruyama, K. Sawada, J. Koike, Strengthening mechanisms of creep resistant  
608 tempered martensitic steel, *ISIJ Int.* 41 (2001) 641–653.
- 609 [39] K. Sawada, M. Bauer, F. Kauffmann, P. Mayr, A. Klenk, Microstructural change of  
610 9% Cr-welded joints after long-term creep, *Mater. Sci. Eng. A.* 527 (2010) 1417–  
611 1426.
- 612 [40] H.G. Armaki, R. Chen, K. Maruyama, M. Igarashi, Creep behavior and degradation  
613 of subgrain structures pinned by nanoscale precipitates in strength-enhanced 5 to 12  
614 pct Cr ferritic steels, *Metall. Mater. Trans. A.* 42 (2011) 3084–3094.

- 615 [41] B.F. Dyson, Continuous cavity nucleation and creep fracture, *Scr. Metall.* 17 (1983)  
616 31–37.
- 617 [42] L. Zhao, H. Jing, L. Xu, J. An, G. Xiao, D. Xu, Y. Chen, Y. Han, Investigation on  
618 mechanism of type IV cracking in P92 steel at 650°C, *J. Mater. Res.* 26 (2011) 934–  
619 943.
- 620 [43] W. Yan, W. Wang, Y.Y. Shan, K. Yang, Microstructural stability of 9–12% Cr  
621 ferrite/martensite heat-resistant steels, *Front. Mater. Sci.* 7 (2013) 1–27.
- 622 [44] T. Shrestha, M. Basirat, I. Charit, G.P. Potirniche, K.K. Rink, Creep rupture  
623 behavior of Grade 91 steel, *Mater. Sci. Eng. A.* 565 (2013) 382–391.
- 624
- 625
- 626